Kinetic Spin-echo Small-angle Neutron Scattering on Non-aqueous Emulsions

Wouter Grünewald

30 March 2023

Supervisors
Dr Wim Bouwman
Dr Steven Parnell
Dr Gregory Smith

This thesis is presented in partial fulfilment of the degree of Master of Science in Applied Physics

Summary

Emulsions, dispersions of one liquid in a second, are ubiquitous in every-day life. Understanding their behaviour is important in many processes, as they are often unstable and undergo ripening. During ripening, the mean size of the emulsion droplets increases due to coalescence and Ostwald ripening. The change in droplet size over time in a decane-in-DMSO emulsion stabilised by Pluronic P-123 surfactant was investigated using spin-echo small-angle neutron scattering (SESANS) and optical microscopy. Rather than measuring the scattering angle using a positionally sensitive detector, as is done in normal SANS, SESANS encodes the scattering angle in the polarisation of the neutron beam, allowing structures at much larger length scales to be probed.

Experiments were done at the ISIS Pulsed Neutron Source and the Reactor Institute Delft to assess the difference between time-of-flight and monochromatic instruments for kinetic SESANS measurements. Using time-of-flight, the cube of the mean radius was found to increase linearly in time with $\frac{\mathrm{d}\bar{R}^3}{\mathrm{d}t} = 25.5\,\mu\mathrm{m}^3\,\mathrm{h}^{-1}$ and the standard deviation of the droplet size distribution increased slightly. Monochromatic SESANS was found to be less appropriate to study kinetics on the order of hours. Using SANS, it was shown that a large number of swollen micelles were present in the emulsion, likely contributing to an increase in Ostwald ripening to above the rate predicted by Lifshitz-Slyozov-Wagner theory. While SESANS can give insight into the increase in droplet size over time, additional techniques are needed to gain a full understanding of which process dominates the ripening.

Preface

This project is part of a long-standing collaboration between ISIS and the TU Delft on the Larmor instrument. The SESANS components have largely been developed in Delft to make use of the full neutron wave length spectrum from the ISIS Target Station 2. I already had an interest in scattering techniques and during my undergraduate degree in Scotland I developed a fondness for the United Kingdom, so when I heard about this collaboration I asked Wim Bouwman if I could do part of my master's thesis with ISIS. Wim and Steven contacted Greg, one of Larmor's instrument scientists, and he proposed to try to measure the evolution of non-aqueous emulsions using SESANS. A proposal for beam time was submitted and just before summer, granted.

From 3 September to 29 November I stayed in Didcot, Oxfordshire and every day I cycled over the hill to Rutherford Appleton Laboratory, where ISIS is located. After practising making emulsions and modelling the expected outcome, we put them on the beamline for the first SESANS experiment. To much confusion, the scattering was much higher than expected. It took a couple days to realise it was because of the surfactant, but after that we were able to collect some good data. The single day of SANS beam time went much more smoothly and afterwards I was able to analyse the data and put it all together.

After returning to Delft, I further analysed the data and repeated the SESANS experiment on the instrument at the Reactor Institute. Taking that additional data into account, I wrote the thesis that you are about to read.

Acknowledgements

The work presented in this thesis would not have been possible without the help of many people. First and foremost I want to thank my supervisors Wim Bouwman, Steven Parnell and Greg Smith for all their help, advice and guidance.
I thank the technicians at ISIS, Diamond Light Source and the Reactor Institute Delft for their amazing support: Sarah Langham, Rachel Pearce, James Taylor, Ludmila Mee, Ann-Kathrin Geiger, Chris Duif, Michel Thijs and Eline van den Heuvel.
I thank Arnout Imhof for the useful discussion on preparing these samples at the start of the project.
I want to thank Sarah Rogers, Rob Dalgliesh, Dirk Honecker, Steve King and the rest of the ISIS SANS team for welcoming me into their group for a couple months.
I thank Monika, Katja, Stan, Eva, Yueer, Biffo, Eveline, Miguel and Stella for their support and company at the Reactor Institute. I also thank Josie for proofreading this thesis.
Last but not least I am incredibly grateful for all my friends and family in Delft, Groningen, Oxfordshire and elsewhere who kept me sane during this project.

Contents

Chapter 1

Introduction

Emulsions are ubiquitous in science, industry and daily life. Applications from making dinner [1] to ordered macroporous materials [2] make the study of emulsion properties an important field. While many emulsions commonly encountered have water as one of their components, non-aqueous (or oil-in-oil) emulsions can have significant benefits in certain applications, such as pharmaceutical delivery and polymer synthesis [3]. For any application, it is important to know quantities like the rheological properties of the emulsion, the droplet size distribution, interactions between droplets and to what extent droplets float or sink to the top/bottom. A number of different methods exist to investigate these properties, such as (electron) microscopy, light scattering, electrical pulse counting, ultrasonic spectrometry and NMR [1]. Each of these has their own particular advantages and disadvantages, so often a combination of techniques is necessary to gain a full understanding of a particular emulsion system.

Another technique to study emulsions is small-angle neutron scattering (SANS). With this technique, structures on length scales between 0.25 and 300 nm can be probed. Because neutrons interact with the nuclei in a system rather than the electron cloud, they can penetrate deep into materials and hence SANS can probe the bulk properties. Neutron techniques are non-destructive and using isotopic labelling, the contrast between different parts of an emulsion can be controlled. Many emulsions, however, have droplets that are larger in size than the range SANS can measure. For systems with dominant length scales in the range of micrometres, ultra-small-angle neutron scattering (USANS) and spin-echo SANS (SESANS) are suitable techniques [4].

In this thesis, the suitability of SESANS to study the evolution of decane-in-DMSO emulsions stabilised by Pluronic P-123 surfactant will be explored. By doing SESANS experiments using both the Larmor instrument at ISIS Pulsed Neutron Source and the SESANS instrument at the Reactor Institute

Delft, the difference between time-of-flight and monochromatic instruments for kinetic measurements will be assessed. This is complemented by SANS and optical microscopy measurements to gain a fuller understanding of the ripening process.

Chapter 2

Emulsions

An emulsion is a dispersion of one liquid into a second, such that the first liquid exists as small droplets in the continuous second [5]. A distinction should be made between macro- and microemulsions. Despite the name, microemulsions typically have droplet sizes smaller than 100 nm, while macroemulsion droplets are in the micrometre range. A more rigorous way to define the difference between these two types of emulsion is by their thermodynamic stability. The change in free energy ΔG_{form} associated with forming the emulsion can be expressed as the sum of the energy change due to the formation of the interface area of the droplets $\Delta A\gamma_{12}$ and the configurational entropy ΔS_{conf} [6].

$$\Delta G_{form} = \Delta A\gamma_{12} - T\Delta S_{conf} \tag{2.1}$$

where T is the absolute temperature, ΔA the change in interfacial area and γ_{12} the interfacial tension between the two liquids. Microemulsions are typically considered thermodynamically stable (and hence have $\Delta G_{form} < 0$), while macroemulsions are merely kinetically stable (and $\Delta G_{form} > 0$).

There are a number of different ways an emulsion can change over time. Creaming and sedimentation are caused by a difference in density between the two liquids. If this is great enough, gravity (or a centrifugal force) will cause the droplets to float to the top or sink to the bottom, depending on whether they are more or less dense than the continuous medium. Flocculation causes droplets to stick together, forming agglomerates. If droplets are very close together, such as in a flocculated cluster, they can also coalesce into a larger droplet. Finally, if the emulsion is polydisperse, i.e. the droplets do not all have the exact same size, the average droplet size can increase due to Ostwald ripening. Flocculation, coalescence and Ostwald ripening are discussed in more detail below.

2.1 Flocculation

In many emulsions, flocculation and coalescence (see figure 2.1) are closely related phenomena. Flocculation is the process whereby droplets associate with each other, but maintain their individual structural integrities [1]. The flocculation rate depends on two factors: the collision rate of the droplets and the probability a collision leads to the droplets sticking together. In the absence of gravitational and shear forces, collisions between droplets are due to Brownian motion. In this case, the collision frequency F_B can be shown to be proportional to the number density n squared with a proportionality constant c_B [1]:

$$F_B = c_B n^2 = \frac{8kT}{3\eta} n^2 = \frac{3kT\phi^2}{2\eta\pi^2 \bar{R}^6} \tag{2.2}$$

where k is Boltzmann's constant, T the absolute temperature, η the viscosity of the continuous phase, ϕ the volume fraction and $\bar{R}$ the mean particle (droplet or floc) radius. The change in the number density over time can then be calculated as [7]:

$$n(t) = \frac{n_0}{1 + (1/2)k_B n_0 t} \tag{2.3}$$

If the flocs are approximately spherical, this implies a linear increase of $\bar{R}^3$ with time. Taking into account the collision efficiency E, this can be written as

$$\bar{R}^3 = \bar{R}_0^3 + \frac{3}{8\pi}\phi F_B E t \tag{2.4}$$

where $\bar{R}_0$ is the mean radius at time $t = 0$.

2.2 Coalescence

If two droplets are in contact with each other for a sufficient period of time, they can coalesce when the film of material separating them (emulsifier membranes and continuous phase) is ruptured. The rate at which droplets grow due to coalescence depends on what process is the limiting step. If coalescence occurs (almost) immediately after droplets come in contact, equation (2.4) can be used and hence $\bar{R}^3$ will increase linearly with time. If the film rupture is the rate-limiting step and the particles are close packed, the mean droplet radius changes as [1]:

$$\frac{1}{\bar{R}^2} = \frac{1}{\bar{R}_0^2} - \frac{4Z}{3} f t \tag{2.5}$$

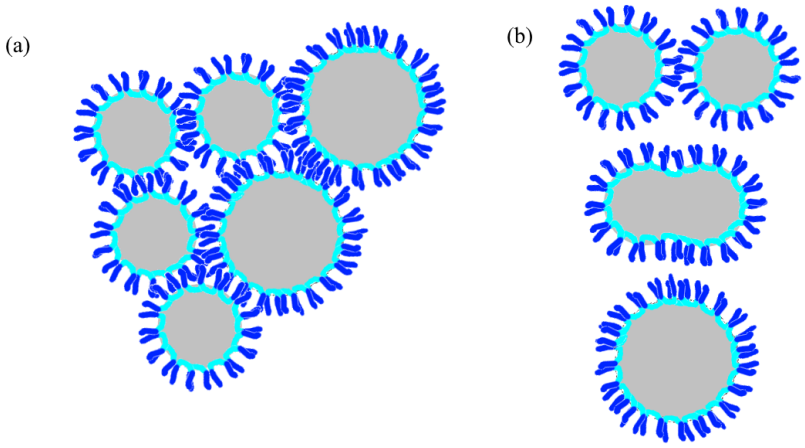

Figure 2.1: (a) Flocculation: multiple droplets stuck together. (b) Coalescence: two droplets in contact merge into a single larger droplet.

where Z is the number of neighbours in contact with every particle and f the frequency of film rupture. If the droplets are not densely packed, this equation has to be changed to

$$\frac{1}{\bar{R}} = \frac{1}{\bar{R}_0} - \frac{Z}{6} f \pi h^* t \tag{2.6}$$

where h^* is the film thickness. So depending on the rate-limiting step and the packing density, coalescence can manifest as a linear change of $\bar{R}^3$, $\frac{1}{\bar{R}^2}$ or $\frac{1}{\bar{R}}$.

2.3 Ostwald Ripening

In emulsion droplets, there exists a pressure difference Δp over the the curved interface between the two liquids [5]:

$$\Delta p = \frac{2\gamma}{R} \tag{2.7}$$

where R is the radius of curvature and γ the interfacial tension. The inverse relation between Δp and R means that the pressure difference is greater for smaller droplets than for larger ones and hence the chemical potential of the molecules in the smaller droplets is greater. If the dispersed liquid is slightly soluble in the continuous one, molecules will diffuse from the smaller droplets to the larger ones due to the difference in chemical potential. This causes small droplets to become smaller and large ones to become larger, as

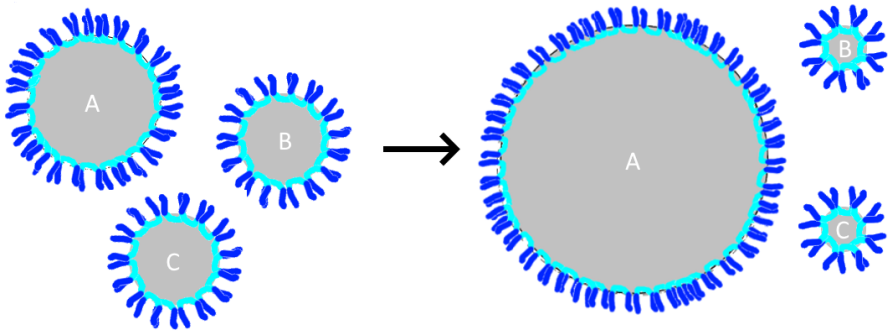

Figure 2.2: Ostwald ripening in an emulsion stabilised by a surfactant. The dark blue part of the surfactant is solvophilic, the light blue part solvophobic. As the pressure difference over the interface is larger in small droplets than in large ones, large droplets (A) tend to grow even larger and smaller droplets (B and C) shrink.

illustrated in figure 2.2. Once droplets become too small, they will dissolve completely and through this process the average droplet size increases.

In surfactant-free conditions, Ostwald ripening is described by Lifshitz-Slyozov-Wagner theory. [8] If the emulsion were infinitely dilute with non-interacting droplets, the cube of the mean radius $\bar{R}^3$ of the emulsion droplets would increase linearly according to [9]

$$\frac{\mathrm{d}\bar{R}^3}{\mathrm{d}t} = \frac{8Dc_\infty\gamma V_m^2}{9\tilde{R}T} \tag{2.8}$$

with D the diffusion coefficient of the dispersed phase in the continuous phase, c_∞ the bulk phase solubility, γ the interfacial tension, V_m the molar volume of the dispersed phase, $\tilde{R}$ the ideal gas constant and T the absolute temperature.

The same theory also implies that a quasi-steady state is established where the size distribution is described by [8, 10]

$$f(u) = \frac{81eu^2\exp\left(2u/3-1\right)^{-1}}{32^{1/3}(u+3)^{7/3}(1.5-u)^{11/3}} \text{ for } u < 1.5 \tag{2.9}$$

and 0 for $u > 1.5$. u is the normalised radius $R/\bar{R}$, e is Euler's number. In practice, most emulsions are better described by size distributions such as a normal, log-normal or Schulz-Zimm distribution [10, 11].

In addition to diffusion, other mass transfer mechanisms may play a role in Ostwald ripening. The surfactant can assist in this process either as loose

molecules or as micelles. The exact mechanism of mass transfer in these cases is not yet well-understood[10]. In some emulsions, a decrease in the ripening rate is observed with increasing surfactant concentration below the critical micelle concentration and an increase in ripening rate at concentrations above that [12, 13]. In other measurements, no clear dependency on the surfactant concentration was observed [14]. Since the change in Ostwald ripening when the surfactant concentration is increased is not the same in different emulsions, the exact mechanism of mass transfer in Ostwald ripening likely depends on many parameters of the system. Important parameters are the surfactant concentration, the volume fraction of the dispersed phase, the characteristics of the two phases and the particular surfactant used.

Chapter 3

Methods

3.1 Materials

The emulsions studied consisted of n-decane in dimethyl sulfoxide (DMSO), stabilised by Pluronic P-123 surfactant. P-123 is a triblock copolymer, consisting of poly(ethylene glycol)-poly(propylene glycol)-poly(ethylene glycol) (PEG-PPG-PEG) chains of 20-70-20 units. The PEG chains are solvophilic and the PPG chain is solvophobic, allowing the molecule to sit on the interface between the decane and DMSO. The hydrogenous and deuterated variants of the solvents were mixed to obtain the desired scattering length density.

3.2 Sample Preparation

The formulation and preparation method of the emulsions was inspired by the work of Imhof and Pine [15]. To prepare the emulsions, first an 18 weight-% solution of P-123 in DMSO was made by melting the surfactant and placing it in a vial. DMSO was added by weight until a solution with the desired concentration was made. The solution was heated to 80 °C until the surfactant was dissolved. 300 µg of this solution was then placed in a vial using a Pasteur pipette and 300 µl of decane was added using volumetric pipettes. This results in an emulsion with an approximate volume fraction ϕ of decane of 0.5. To minimise the scattering from the surfactant, hydrogenous and deuterated DMSO were mixed such that the average scattering length density was close to that of P-123 (0.424×10^{-6} Å^{-2}). If this is not done, it becomes very difficult to control the scattering contrast between the decane and the continuous phase. The scattering length density of the continuous phase is the average of that of DMSO and the fraction of the surfactant not on the surface of a droplet. Since this second quantity is unknown, the contrast

Sample	ρ_{DMSO} (10^{-6} Å^{-2})	ρ_{decane} (10^{-6} Å^{-2})	$\Delta\rho$ (10^{-6} Å^{-2})
Larmor 1	0.453	0.798	0.345
Larmor 2	0.453	0.818	0.365
Larmor 3	0.453	0.845	0.392
Delft	0.453	1.41	0.687
SANS	5.28	5.17	0.11

Table 3.1: Scattering length densities of the different emulsions made.

can be wildly different to what one might expect. The ratio of hydrogenous to deuterated decane was chosen such that the contrast was small enough as to not depolarise the neutron beam completely, but large enough to give sufficient signal. The exact values are given in table 3.1.

The mixture was then emulsified by shaking. The vial was shaken by hand for 20 seconds and then using a mechanical 25 Hz shaker for 20 seconds. This was repeated three times, after which the emulsion was allowed to rest for a short time. The emulsion was then alternately mechanically shaken and allowed to rest until a very viscous emulsion was formed.

The emulsion was then placed in a cylindrical quartz cuvette with a 1 mm path length using a syringe. This type of cuvette was used so a large diameter neutron beam could be used. To prevent creaming, the cuvettes were placed in a non-ferrous rotating sample rack.

In addition to the emulsions, solutions of 1, 5, 10 and 18% P-123 in deuterated DMSO were prepared to measure using SANS.

3.3 Optical Microscopy

The emulsions were studied using a Zeiss Axioscope 7 optical microscope with 5x to 100x magnification. Digital images were taken using the Axiocam 208c camera attachment in both bright-field and dark-field modes. The microscope was provided by Diamond Light Source Ltd., Rutherford Appleton Laboratory, Oxfordshire. To prepare an emulsion suitable for microscopy, the prepared solution had to be diluted in DMSO prior to placing a drop on a glass slide. The emulsion was then covered by a glass cover slip and placed under the microscope. The Hough transform included in Fiji ImageJ [16] was used to analyse the images and obtain a size distribution.

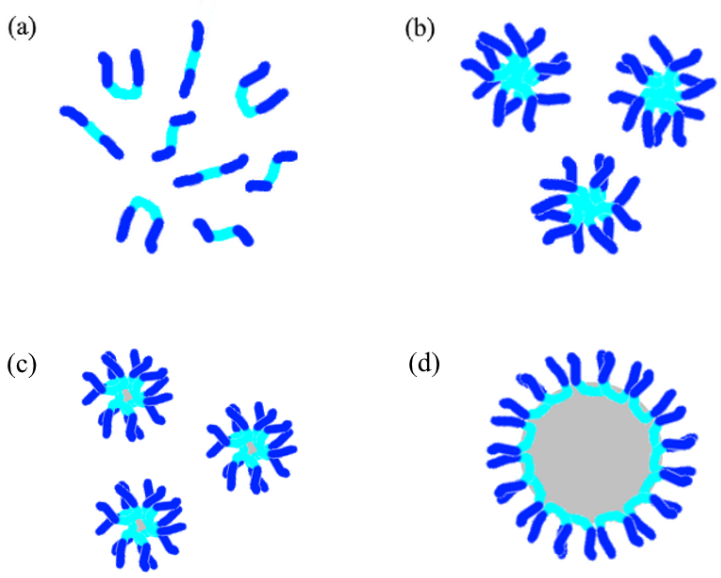

Figure 3.1: Different structures present in the surfactant solutions and emulsions. The light and dark blue represent the solvophobic PPG and solvophilic PEG blocks of P-123, respectively. (a) Loose polymer chains; (b) Micelles; (c) Micelles swollen with decane; (d) Decane emulsion droplets. The polymer chains and micelles are on the order of nanometres, while the emulsion droplets are micrometre sized.

3.4 SANS

Since scattering techniques typically provide information in reciprocal space, one needs to measure scattering at smaller angles when investigating larger structures. Hence, small-angle neutron scattering (SANS) is a powerful technique to study the nanometre-scale structures found in soft matter and colloids. The coherent elastic scattering cross section in a solid angle Ω for a system of nuclei j with scattering length b_j is

$$\frac{\mathrm{d}\sigma}{\mathrm{d}\Omega} = \left| \sum_j b_j \exp(i\mathbf{q} \cdot \mathbf{r}_j) \right|^2 \tag{3.1}$$

where $\mathbf{q} = \mathbf{k}_f - \mathbf{k}_i$ is the scattering vector (assuming elastic scattering), defined as the difference between the wave vectors before and after scattering. The scattering vector $\mathbf{q}$ can be related to the scattering angle and the wavelength by $q = 4\pi \frac{\sin\theta}{\lambda}$.

For scattering from large particles into small angles (and therefore small values of $\mathbf{q}$), the volume-specific cross section (commonly denoted as the scattered intensity $I(q)$) can be written as

$$I(q) = \phi(\Delta\rho)^2 V S(\mathbf{q}) P(\mathbf{q}) \tag{3.2}$$

where ϕ is the particle volume fraction, $\Delta\rho$ is the contrast in scattering length density between the particles and the solvent and V is the particle volume. The particle form factor $P(\mathbf{q})$ can be written as

$$P(\mathbf{q}) = \left| \frac{1}{V} \int e^{i\mathbf{q}\cdot\mathbf{r}} \mathrm{d}V \right|^2 \tag{3.3}$$

The structure factor $S(\mathbf{q})$ depends on the long-range structure between particles. In the case of isotropic interactions between many particles, it can be written as

$$S(q) = 1 + 4\pi \frac{N}{V_t} \int_V (g(r) - 1) r^2 \frac{\sin qr}{qr} \mathrm{d}r \tag{3.4}$$

where N is the number of particles, V_t the total volume and $g(r)$ the pair correlation function. For dilute systems, the structure factor approaches unity and can typically be neglected, while it must be taken into account for more concentrated systems. The pair correlation function often cannot be calculated exactly and so approximations must be used to find an expression.

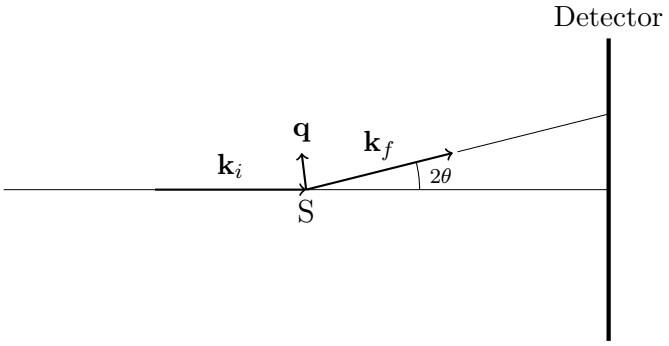

Figure 3.2: The basics of SANS. In coming neutrons with wave vector $\mathbf{k}_i$ are scattered by the sample S with an angle 2θ. The scattering angle and therefore the wave vector after scattering $\mathbf{k}_f$ is measured by the position of the neutron on the detector. The scattering vector $\mathbf{q} = \mathbf{k}_f - \mathbf{k}_i$ can be related to the angle 2θ as $q = 4\pi\frac{\sin\theta}{\lambda}$.

3.4.1 Models

In the SANS experiment, both loose polymer chains and self-assembled micelles are visible. The chains can be approximated as Gaussian coils, for which Debye [17] calculated the scattering as

$$I(q) = I_0 2\frac{\exp(-u) + u - 1}{u^2} \tag{3.5}$$

$$u = q^2 R_g^2 \tag{3.6}$$

where I_0 is the scattered intensity at $q = 0$ and R_g is the radius of gyration.

The micelles can be fitted with the `SPHERE+Chains(RW)` model in SASfit [18]. This model can be written in terms of the self-correlation of the core, the brush, the cross term between the core and chains and the cross term between the different chains:

$$\begin{aligned} I_{mic} =& N_{agg}^2\beta_{core}^2 P_{core}(q) + N_{agg}\beta^2 P_{brush}(q) \\ &+ 2N_{agg}^2\beta_{core}\beta_{brush}S_{brush-core}(q) + N_{agg}(N_{agg}-1)\beta_{brush}^2 S_{brush-brush}(q) \end{aligned} \tag{3.7}$$

where

$$\begin{aligned}
\beta_{brush} &= V_{brush}(\rho_{brush} - \rho_{solv}) \\
\beta_{core} &= \frac{V_{core}(1 - x_{solv,core})}{N_{agg}}(\rho_{core} - \rho_{solv}) \\
P_{core}(q, R_{core}) &= \Phi^2(qR_{core}) \\
\Phi(qR) &= 3\frac{\sin(qR) - qR\cos(qR)}{(qR)^3} \\
P_{brush}(q, R_g) &= 2\frac{\exp(-x) - 1 + x}{x^2} \text{ with } x = R_g^2 q^2 \\
S_{brush-core}(q, R_{core}, R_g, d) &= \Phi(q, R_{core})\psi(qR_g)\frac{\sin\left(q(R_{core} + dR_g)\right)}{q(R_{core} + dR_g)} \\
\psi(qR_g) &= \frac{1 - \exp(-x)}{x} \\
S_{brush-brush}(q, R_{core}, d, R_g) &= \psi^2(qR_g)\left(\frac{\sin(q(R_{core} + dR_g))}{q(R_{core} + dR_g)}\right)^2
\end{aligned}$$

The parameters of the implemented model are the radius of the micellar core R_{core}, the grafting density (copolymer molecules N_{agg} per unit surface S) n_{agg}, the molecular volume of the part of the polymer forming the corona V_{brush}, the radius of gyration of the block unit in the corona R_g and the scattering length densities of the core, brush and solvent (calculated to be 0.34, 0.64 and $5.28 \times 10^{-6}\,\text{Å}^{-2}$ respectively). $x_{solv,core}$ is the amount of solvent in the core and d is the non-penetration of the chains into the core, assumed to be equal to 1. A hard-sphere structure factor was also applied with a radius R_{HS} and volume fraction ϕ.

3.5 SESANS

If the length scales of interest are on the order of micrometres rather than nanometres, the corresponding scattering angles are so small they are indistinguishable from the direct beam. One method to avoid this problem is to encode the scattering angle in the polarisation of a neutron beam. Spin-echo small-angle neutron scattering (SESANS) achieves this using magnetic field regions with inclined faces relative to the incoming neutron beam [19]. If a polarised neutron passes through a magnetic field, its spin will precess. The precession angle is

$$\varphi = c\lambda BL \tag{3.8}$$

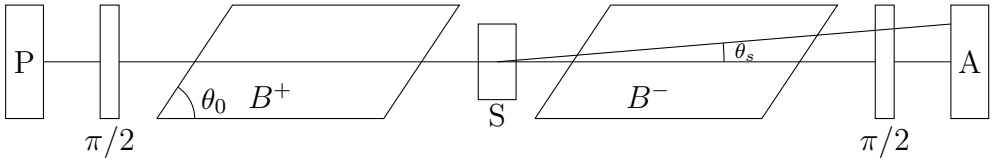

Figure 3.3: Layout of a Spin-Echo SANS experiment. Incoming neutrons are polarised at P and flipped into the precession plane by a $\pi/2$-flipper. The beam then passes through two magnetic field regions with opposite sign and faces with angle θ_0 relative to the incident beam. Before being analysed at A, the neutron spins are flipped back by another $\pi/2$-flipper. If no scattering occurs at the sample S, the Larmor precession in the two field regions cancel each other out. When a neutron is scattered by the sample, a net precession effect can be measured as a partial depolarisation of the beam.

where $c = 4.6368 \times 10^{14}\,\mathrm{T^{-1}\,m^{-2}}$, λ the neutron wavelength, B the magnetic field strength perpendicular to the spin and L the path distance of the neutron through the magnetic field.

By using a configuration as given in figure 3.3, the Larmor precession can be used to encode the scattering angle. The precession of a neutron with a transmission angle θ with the x-axis through a region with field B over length L is

$$\varphi = c\lambda BL\frac{\sin\theta_0}{\sin(\theta_0+\theta)} \cong c\lambda BL(1+\theta\cot\theta_0) \tag{3.9}$$

with θ_0 the angle of the magnetic field regions with the beam axis. If the neutron traverses two of these magnetic field regions with opposite magnetic fields without changing its angle θ with the x-axis, the precession in the two regions exactly cancel each other out. However, if the neutron is now scattered by a sample placed between the two magnetic fields by an angle θ_s, the precession difference is

$$\Delta\varphi \approx c\lambda BL\theta_s\cot(\theta_0) \equiv \delta q \tag{3.10}$$

where

$$\delta = \frac{c\lambda^2 L\cot(\theta_0)}{2\pi}B \tag{3.11}$$

$$q = \frac{2\pi\theta_s}{\lambda} \tag{3.12}$$

δ is known as the spin-echo length and q is the scattering vector. After the precession regions, the final polarisation of the beam is measured:

$$\frac{P(q,\delta)}{P_0} = \cos(\Delta\varphi) = \cos(\delta q) \tag{3.13}$$

Where $P(q, \delta)$ is the polarisation measured with the sample in the beam and P_0 that of the empty beam without a sample. During a SESANS experiment, the final polarisation of the neutron beam is measured at different spin-echo lengths. This is done by changing one or more of the parameters in equation (3.11). At a pulsed neutron source, such as ISIS, the neutron wavelength can be determined from the time difference between the moment the neutrons are emitted by the moderator and their detection. This allows the polarisation to be measured at many wavelengths, and therefore many spin-echo lengths, at the same time. At continuous sources, such as the reactor in Delft, the neutrons pass through a monochromator and hence only one spin-echo length is probed at a time. The magnetic field strength is then changed to measure the polarisation at different spin-echo lengths.

The normalised polarisation of the neutron beam can be calculated from the scattering cross section by [20]

$$\frac{P(\delta)}{P_0} = e^{\lambda^2 t(G(\delta)-G(0))} \tag{3.14}$$

where t is the sample thickness and

$$G(\delta) = \frac{1}{2\pi}\int_0^\infty J_0(q\delta)I(q)q\mathrm{d}q \tag{3.15}$$

$$G(0) = (\Delta\rho)^2\phi(1-\phi)\xi \tag{3.16}$$

in which J_0 is a zeroth order Bessel function of the first kind and $I(q)$ is the scattering cross section as measured in conventional SANS. ξ is the correlation length of the system and $G(\delta)$ is a two-dimensional projection of the 3D correlation function $\gamma(r)$ [21], known as the absolute scattering correlation function. To obtain a quantity independent of the wavelength used by the instrument and the thickness of the sample, the reduced polarisation is defined as

$$\frac{\ln(P/P_0)}{\lambda^2 t} = (G(\delta) - G(0)) \tag{3.17}$$

Since $G(\delta)$ falls to 0 for large δ (in the absence of long-range order), the reduced polarisation will fall from 0 at $\delta = 0$ to a plateau at $-(\Delta\rho)^2\phi(1-\phi)\xi$. The spin-echo length at which this plateau is reached is also indicative of the dominant length scale of the system.

3.5.1 Models

The data obtained from the SESANS experments can be interpreted in a number of different ways. One could calculate the SESANS signal directly

from the 3D correlation function. However, this can quickly become very complex, especially if a (polydisperse) structure factor has to be taken into account [22]. Instead, the reciprocal space SANS model can be calculated and converted to a SESANS signal using a numerical Hankel transform. This is implemented in SasView, allowing the full library of SANS models to be easily used for SESANS [23]. Below, the relevant reciprocal space models will be discussed.

The emulsions under investigation are concentrated systems of polydisperse particles, so some assumptions and simplifications have to be made in the models fitted to the data. If the emulsion droplets are assumed to be spherical, the well-known particle form factor for spheres can be used: [24]

$$P(q,R) = F^2(q,R) = \left(3\frac{\sin(qR) - qR\cos(qR)}{(qR)^3}\right)^2 \tag{3.18}$$

This form factor applies to spherical particles with radius R. If the radius is polydisperse, the scattering intensity can be calculated by [25]

$$P(q) = \frac{scale}{V}\int_{\mathbb{R}^+} f(x;\mu,\sigma)F^2(q,x)\mathrm{d}x \tag{3.19}$$

where $f(x;\mu,\sigma)$ is a particle size distribution. For emulsions, this is commonly described by a log-normal distribution [26]. Such a distribution is a function of x where $\ln(x)$ is normally distributed. It is given by

$$f(x;\mu,\sigma) = \frac{1}{x\sigma}\exp\left(-\frac{1}{2}\left(\frac{\ln(x)-\mu}{\sigma}\right)^2\right) \tag{3.20}$$

with μ and σ the mean and standard deviation of the underlying normal distribution. The mean of the log-normal distribution is given by

$$\bar{x} = e^{\mu+\frac{\sigma^2}{2}} \tag{3.21}$$

and the variance by

$$v = \left(e^{\sigma^2}-1\right)e^{2\mu+\sigma^2} \tag{3.22}$$

Since the emulsion droplets have a volume fraction ϕ of approximately 0.5, the interaction between droplets has to be taken into account by means of a structure factor. The structure factor can be calculated according to equation (3.4) from the pair correlation function $g(r)$. This can be found as a solution to the Ornstein-Zernike equation [27]

$$h(r) = c(r) + \rho\int c\left(|\mathbf{r}-\mathbf{r}'|\right)h(r')\mathrm{d}\mathbf{r}' \tag{3.23}$$

where $h(r) = g(r) - 1$ is the *total correlation function* and $c(r)$ is the *direct correlation function*. Since both of these functions are unknown, an additional closure relation is needed to solve this equation. Such a closure relation can be found if certain assumptions or approximations of the physical system can be made. A simple approximation assumes the droplets behave like hard spheres, with no interaction at inter-particle distances r greater than twice the radius of the particles and an infinitely strong repulsive potential at distances smaller than that. In this case, the Percus-Yevick closure relation [28] can be used:

$$c(\mathbf{r}) \approx (1 - e^{\frac{v(\mathbf{r})}{k_B T}}) g(\mathbf{r}) \tag{3.24}$$

with $v(\mathbf{r})$ the potential between particles. From this, the structure factor can be calculated [29]:

$$S_{HS}(q, R_{HS}, \phi) = \frac{1}{1 + 24\phi \frac{L(\phi, A)}{A}} \tag{3.25}$$

with

$$\begin{aligned} L(\phi, A) =& \alpha \frac{\sin A - A\cos A}{A^2} + \beta \frac{2A\sin A + (2 - A^2)\cos A - 2}{A^3} \\ &+ \gamma \frac{-A^4 \cos A + 4\left((3A^2 - 6)\cos A + (A^3 - 6A)\sin A + 6\right)}{A^5} \end{aligned}$$

where

$$\begin{aligned} A =& 2R_{HS}q \\ \alpha =& \frac{(1 + 2\phi)^2}{(1 - \phi)^4} \\ \beta =& -6\phi \frac{(1 + \phi/2)^2}{(1 - \phi)^4} \\ \gamma =& \frac{\phi\alpha}{2} \end{aligned}$$

To account for the polydispersity in the structure factor, the beta decoupling approximation is used [30]. The scattering intensity is then calculated as

$$I(q) = \text{scale} \frac{\mathrm{V_f}}{\mathrm{V}} \mathrm{P(q)} \left(1 + \beta(\mathrm{q})(\mathrm{S(q)} - 1)\right) \tag{3.26}$$

where β is given by

$$\beta(q) = \frac{|\langle F(q) \rangle|^2}{\langle |F(q)|^2 \rangle}$$

3.6 Instruments

3.6.1 Larmor

Larmor is a combined SANS and SESANS instrument at the ISIS Pulsed Neutron Source at Rutherford Appleton Laboratory, Oxfordshire. Neutrons are produced using an intense proton beam accelerated by a synchrotron. The protons hit a tungsten/tantalum target, during which neutrons are produced through spallation. The neutrons are moderated (i.e. their kinetic energy decreased and their wavelength increased) using cold hydrogen and methane moderators. The wavelength of the neutrons can be determined from the time difference between the emission time of the neutrons from the moderator and their detection by

$$\lambda = \frac{h\Delta t}{m_n d} \tag{3.27}$$

where h is Planck's constant, Δt the time difference, m_n the mass of a neutron and d the distance between the target and the detector. Larmor implements a SESANS setup as described in section 3.5 using adiabatic RF flippers to realise the effect of parallelogram-shaped magnetic field regions [31]. This, combined with the time-of-flight technique to determine the neutron wavelength, allows Larmor to operate using a wide range of neutron wavelengths (2.6 to 10 Å). The different spin-echo lengths are therefore probed by varying λ in equation (3.11). The RF flippers can be operated at 0.5, 1.0 or 2.0 MHz, corresponding to magnetic fields of 17.14, 34.28 and 68.56 mT respectively. The poleshoe angle (θ_0 in equation (3.11)) can be varied between 20° and 89°. The length of the precession regions is approximately 1.5 m and a known grating is used to calibrate the instrument. Before every measurement, the instrument needs to be tuned to ensure it is on echo. This is done by scanning a tuning coil close to the sample position, as can be seen in figure 3.5. For the experiments described in this thesis, a frequency of 2.0 MHz and $\theta_0 = 30°$ were chosen.

Larmor can also be operated as a conventional SANS instrument with a sample-to-detector distance of 4 metres and a 64 x 64 cm^2 detector. With neutrons between 0.5 and 12.5 Å this gives a q range of 0.005 to 0.7 $Å^{-1}$.

3.6.2 Delft SESANS

The SESANS at the Reactor Institute Delft is a monochromatic instrument using thermal (1.93 Å) neutrons produced by a 2.3 MW nuclear reactor. It uses magnetised foils to implement the shaped magnetic field regions necessary for spin-echo labelling. While they only work for one specific wavelength, these foils are much simpler than the RF system used on Larmor and much

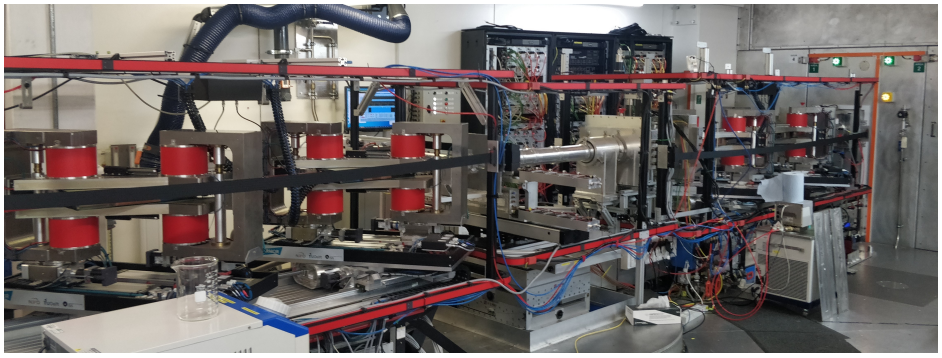

Figure 3.4: The Larmor instrument at ISIS Pulsed Neutron Source, Rutherford Appleton Laboratory, Oxfordshire. The instrument can be used in both spin-echo and conventional SANS modes.

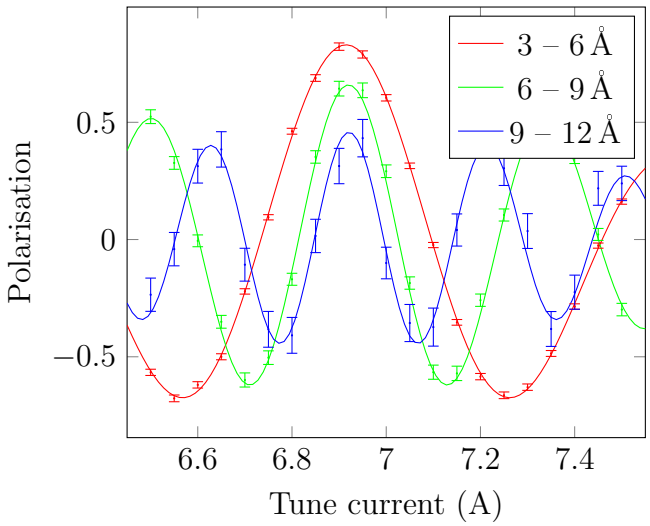

Figure 3.5: An echo scan on Larmor to tune the instrument. When the three curves (corresponding to different wavelengths) have a maximum at the same value of the tune coil, the instrument is on echo for all wavelengths. Here, the echo point was found to be at a tune coil setting of 6.919 A, so the coil was set to that value for the measurement.

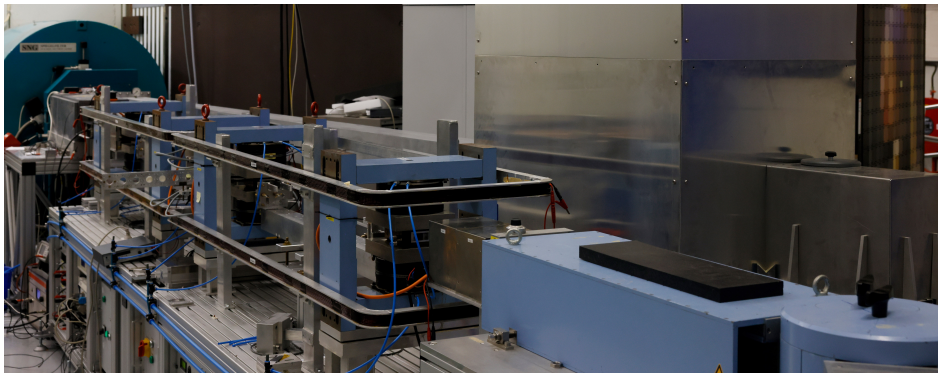

Figure 3.6: The SESANS instrument at the Reactor Institute Delft.

smaller angles of the magnetic precession regions ($\theta_0 = 5.5°$) can be achieved. The length of the precession regions is 1.340 m, and the magnetic field was scanned from 10 to 190 mT. During a measurement, the guide field around the second precession arm is varied slightly to bring the instrument on and off echo (see figure 3.7). A function is then fitted of the form

$$I = I_{shim}\left(1 + P\sin\left(2\pi\frac{x}{T} - \Delta\right)\right) \tag{3.28}$$

with x the current through the guide field coil. The polarisation is given by the amplitude $P = \frac{I_{pol}}{I_{shim}}$.

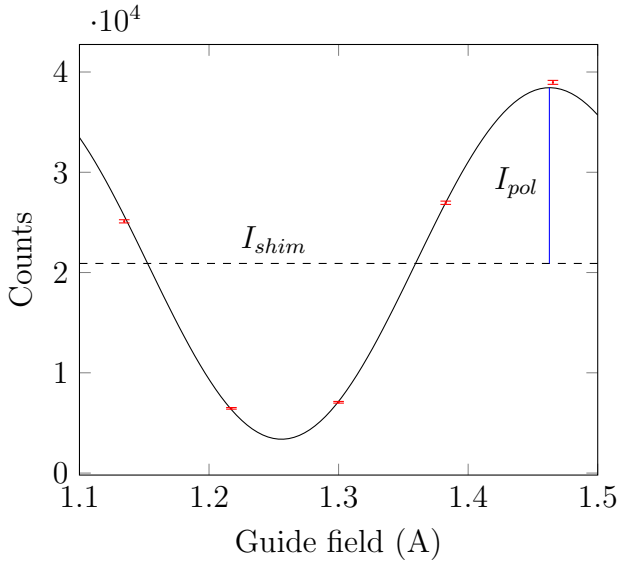

Figure 3.7: Raw data from a Delft SESANS measurement fitted with a function according to equation (3.28). For this spin-echo length, the shim intensity $I_{shim} = 20509$ counts and the polarisation was found to be 0.84.

Chapter 4

Results and discussion

The emulsions were prepared and left on the lab bench for observation (figure 4.1). The formed emulsion was very viscous and showed strong creaming. If left to rest, they showed good stability over multiple days, likely because the decane was trapped in the dense fluid and could not float to the top.

4.1 Microscopy

Microscopy images of the prepared emulsion were taken at different times. As can be seen in figure 4.2, the droplets are smaller shortly after preparation than in the aged emulsion. Two different samples were made according to the same procedure to assess the reproducibility. In photo 4.2b, many small droplets are visible in the background of the larger ones.

For sample 2, histograms were made for the size distribution after 1 and 4 hours (figure 4.3). A clear increase in mean size is visible (from 1.7 to 4.1 µm) and a slight increase in the width of the distribution. It should be noted that obtaining quantitative data from these images in a systematic way is very difficult, since the low resolution and large number of imaging artefacts make it difficult for the Hough transform algorithm to measure the droplets accurately. In many cases, not all droplets were detected while at the same time a considerable number of imaging artefacts were incorrectly identified as emulsion droplets. Furthermore, the distribution was not the same when different images of the same emulsion (taken at the same time) were analysed. This, in combination with computational limitations, makes the quantitative results unreliable.

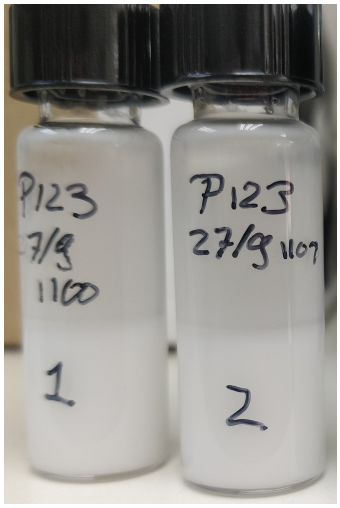

(a) 1 hour after preparation.

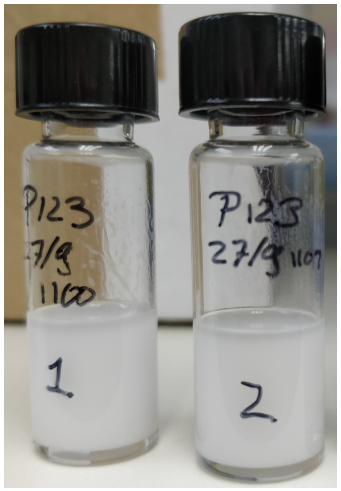

(b) 27 hours after preparation.

Figure 4.1: The prepared emulsions were viscous and showed quick creaming. Left for observation, they appeared relatively stable for multiple days.

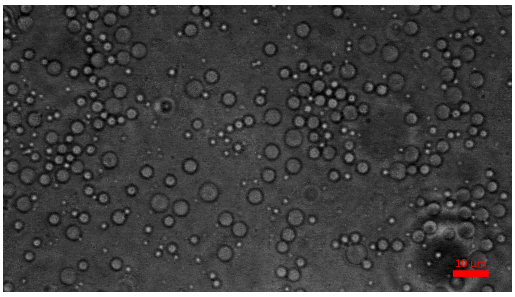

(a) P-123 sample 1 after 3 hours.

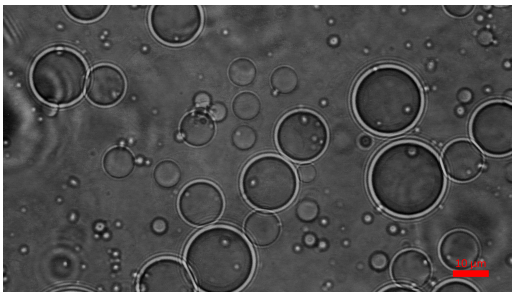

(b) P-123 sample 1 after 20 hours

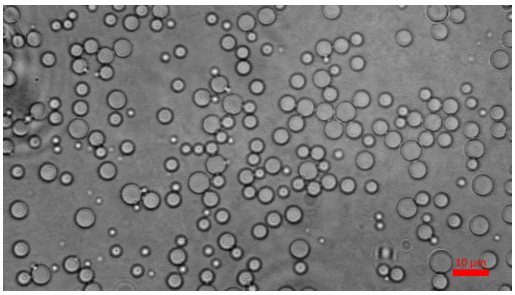

(c) P-123 sample 2 after 1 hour

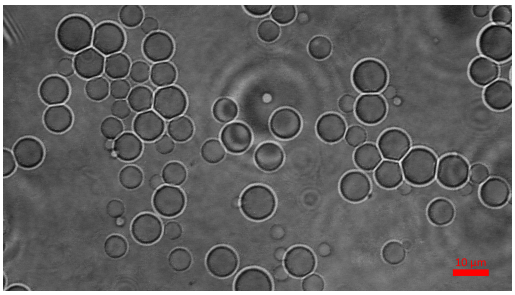

(d) P-123 sample 2 after 4 hours

Figure 4.2: Optical microscopy images of decane-in-DMSO emulsions. Two different samples were prepared according to the same recipe. The scale bars are 10 µm.

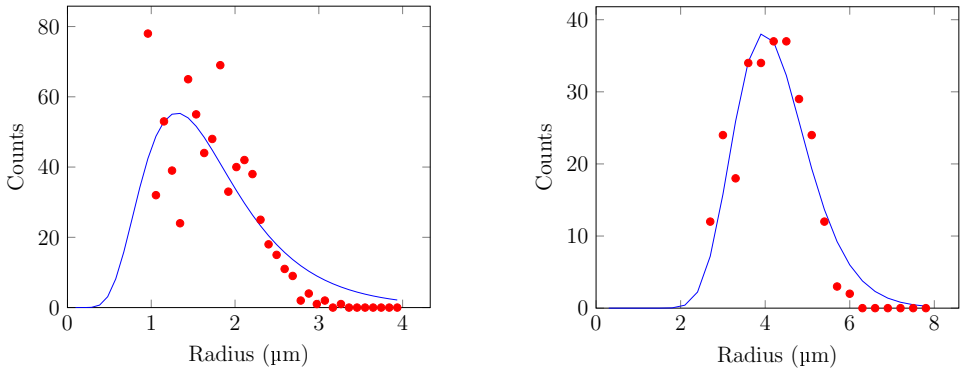

(a) Sample 2 after 1 hour. The mean and standard deviation of the log-normal distribution are 1.7 µm and 0.8 µm respectively.

(b) Sample 2 after 4 hours. The mean and standard deviation of the log-normal distribution are 4.1 µm and 0.9 µm

Figure 4.3: Histograms of sample 2 after 1 and 4 hours. A log-normal distribution was fitted to the observed droplet counts.

4.2 SANS

In figure 4.4a, the SANS signal for a 1% solution of P-123 is plotted with a mono-gauss model fit. The loose polymer chains were found to have a radius of gyration $R_g = 35.9\,\text{Å}$. In figure 4.4b, the signals for 5, 10 and 18% solutions are plotted, fitted with a spherical micelle model `SPHERE+chains(RW)`. The results from simultaneously fitting these curves are given in table 4.1. From the fact that a micelle model cannot be fitted to the 1% solution, and vice-versa that a mono-gauss model cannot explain the curves for higher concentrations, we can conclude that the critical micelle concentration of P-123 in d-DMSO is between 1 and 5 wt-%. Since the decane-in-DMSO emulsions measured are all made with a high-concentration solution of surfactant, these micelles will be present in the emulsions and can affect the behaviour.

In figure 4.5, the SANS signal from such an emulsion can be seen together with the signal from the 18% surfactant solution. The ratio of deuterated to hydrogenous decane was chosen such that the SLD of the decane was close to that of d-DMSO, so as to more clearly see the effects of the surfactant. This curve was fitted with the same `SPHERE+chains(RW)` model as before, but now allowing for the micelles to be swollen with decane. This swelling explains the shift of the structure factor peak towards lower q. The corresponding hard-sphere radius increases from 62.0 Å to 85.5 Å (see table 4.1).

	Surfactant micelles			Emulsion
	5%	10%	18%	
ϕ	0.058	0.173	0.276	0.302
R_{HS}(Å)	62.0			85.5
R_{core}(Å)	6.6			*
$x_{solv,core}$	*0*			*0.95*
n_{agg}(Å^{-2})	0.061			
V_{brush}(Å^3)	*1463* [33]			
R_g(Å)	20.8			

Table 4.1: Parameters of the `SPHERE+chains` model. Numbers in roman type were simultaneously fitted, numbers in italics estimated or calculated.
* Fitted with a log-normal distribution with $\bar{R} = 15.9\,\text{Å}$ and $\sigma = 0.31$.

In addition to the scattering from the surfactant micelles, which are on the order of nanometres, there is also a contribution from the micrometre-sized emulsion droplets. This gives a steep slope at low values of q. This was accounted for in the model by a q^{-4} contribution, since the droplets are large enough that the scattering from these can be assumed to behave according to Porod's law in the entire SANS range [32]. In this limit, the intensity decreases proportionally to q^{-4} as

$$I(q) = 2\pi(\rho)^2 \Sigma q^{-4} \tag{4.1}$$

where Σ is the specific area (i.e. droplet surface per unit volume). This is related to the typical radius of spherical droplets R as

$$R = \frac{3\phi}{\Sigma} \tag{4.2}$$

In figure 4.6, the scattering from the emulsion droplets is visible below $q = 0.01\,\text{Å}^{-1}$. Although this is in the low-q regime for the scattering from the surfactant micelles, it can be considered to be in the high-q region for the scattering from the emulsion droplets, since these are so much larger. The decrease in intensity over time visible in figure 4.6 is therefore related to a decrease in specific area of the emulsion droplets and hence an increase in mean radius.

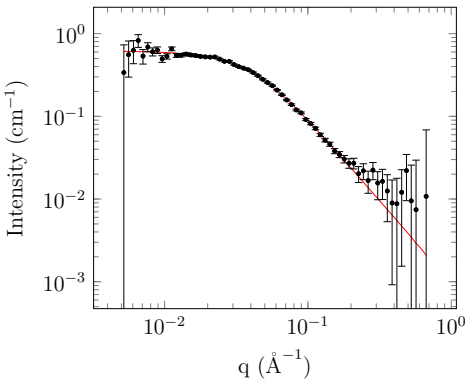

(a) The SANS curve from 1% Pluronic P-123 in deuterated DMSO. A mono-gauss coil was fitted with a radius of gyration of 35.9 Å ($\pm$0.3, $\chi^2 = 0.77$).

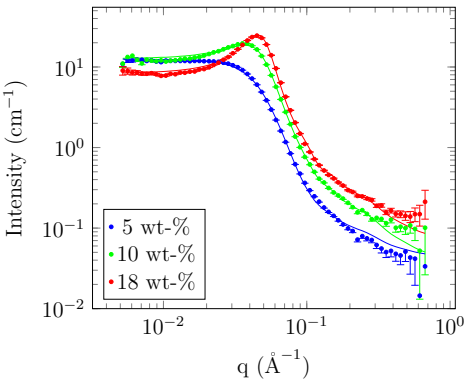

(b) The SANS curves for 5, 10 and 18% P-123 in deuterated DMSO. The three datasets were simultaneously fitted using a polymer micelle model.

Figure 4.4: Results of the SANS measurements on P-123 solutions in deuterated DMSO. The critical micelle concentration is found to be between 1 and 5%.

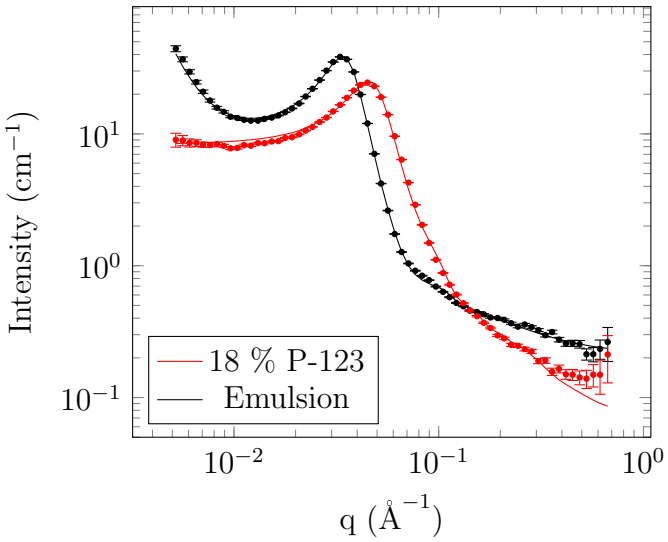

Figure 4.5: SANS data from a decane-in-DMSO emulsion compared to that from 18% P-123 micelles. The shift of the peak to lower q indicates an increase of the micelle size, likely due to the micelles being swollen with decane.

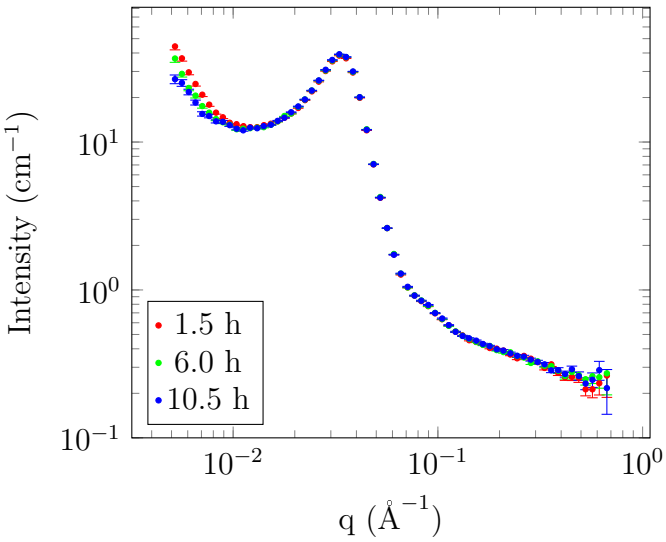

Figure 4.6: Emulsion SANS measurements taken at different ages of the emulsion. The peak from the swollen micelles stays the same, while the intensity at low q becomes lower. Since the entire SANS range can be considered to be in the Porod limit for the micrometre-sized emulsion droplets, this indicates a decrease in specific volume and hence an increase in the mean droplet radius.

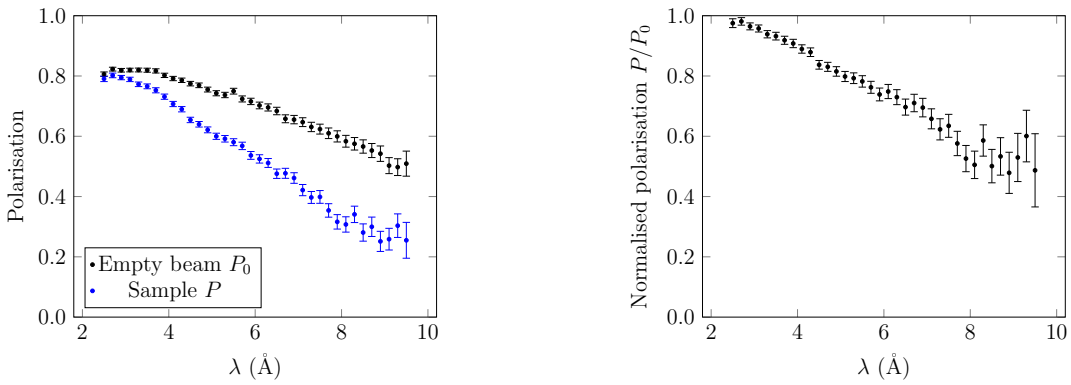

Figure 4.7: The polarisation data obtained on Larmor for a sample (P) and the empty beam (P_0) (left) and the normalised polarisation P/P_0 (right).

4.3 SESANS

4.3.1 Data reduction and fitting

On Larmor, the polarisation as a function of wavelength was measured. This was done for both the sample (P) and the empty beam (P_0), so that the normalised polarisation P/P_0 could be calculated. The polarisations for one measurement can be seen in figure 4.7. If the polarisation of the sample is lower than approximately 0.2, the data becomes unreliable and cannot be used. Additionally, if the measurement time is very short, the polarisation signal can become erratic at higher wavelengths. Due to this, only data obtained at wavelengths smaller than 8.0 Å was used in the analysis, even though the measurement used neutrons up to 12.0 Å. The natural log of the normalised polarisation is divided by the wavelength squared and the thickness of the sample to obtain the SESANS signal.

Three emulsions were measured, denoted as sample 1, 2 and 3. The three samples were prepared identically apart from a small difference in the scattering length density of the decane. Every 10 minutes, a new measurement was started to track the change over time. At later times, the change in droplet radius was slower so multiple runs could be summed together to improve the statistics. Due to a trip of the ISIS proton accelerator, the neutron beam was not in operation during a significant portion of the measurement of sample 2 and hence the results had to be discarded.

The models described in section 3.5.1 are implemented in the software package SASview [34]. This software was used to fit the obtained SESANS

data with the Levenberg-Marquardt algorithm. The volume fraction ϕ of the decane droplets was assumed to be 0.5 and the droplet radius, polydispersity (i.e. σ) and a scale factor were fitted to the data. The data and fits for three different time points are given in figure 4.8. At later times, the mean radius of the droplets becomes larger. This is reflected in the SESANS data by the saturation plateau starting at higher spin-echo length and being at higher depolarisation (i.e. the SESANS signal is more negative). One of the effects of the polydispersity is to dampen out the oscillations in the structure factor, so the visiblilty of oscillations in the signal indicates a small relative polydispersity ($\sigma \approx 0.15$ in equation (3.20)).

The experiment was repeated on the SESANS instrument at the Reactor Institute Delft. Since the Delft instrument is monochromatic, the magnetic field strength has to be varied to measure the depolarisation at different spin-echo lengths. This, in addition to the weaker scattering at smaller wavelengths, makes the measurement take longer and hence the temporal resolution is lower. To obtain a resolution of 33 minutes per full measurement, only ten spin-echo lengths were measured. The results for some time points can be seen in figure 4.9, where the signal is compared against the measurements taken on Larmor. The two measurements broadly agree, although the the statistical information of the data obtained at ISIS is considerably higher than in Delft.

4.3.2 Growth behaviour

Depending on the growth mechanism, the mean radius of the particles changes differently in time. Flocculation, coalescence rate-limited by collisions and Ostwald ripening all give a linear increase of $\bar{R}^3$ in time. If the film rupture between particles is the rate-limiting step in coalescence, $\frac{1}{\bar{R}^2}$ or $\frac{1}{\bar{R}}$ decreases linearly. From the fits to the SESANS signal, the mean radius was obtained and the cube is plotted in figures 4.10 and 4.11. The results from the SESANS measurements show a clear linear trend of $\bar{R}^3$ with time. The rate of the coarsening can be determined by fitting a line. As can be seen in figures 4.10 and 4.11, the ripening rate of the emulsions is approximately $25.5\,\mu m^3\,h^{-1}$.

Two other parameters were fitted: a scale factor and the polydispersity. Ideally, the scale factor should be equal to $(1 - \phi)$, i.e. 0.5. However, the approximations used in calculating the structure factor may become less accurate as the concentration increases. The work by Ashcroft and Lekner [29] on liquid metals shows that at high concentrations, the oscillations of the Percus-Yevick approximation fall out of phase with the real signal. This, combined with the fact that the volume fraction in these emulsions is not known exactly, will cause the scale to differ from the ideal value. As can be

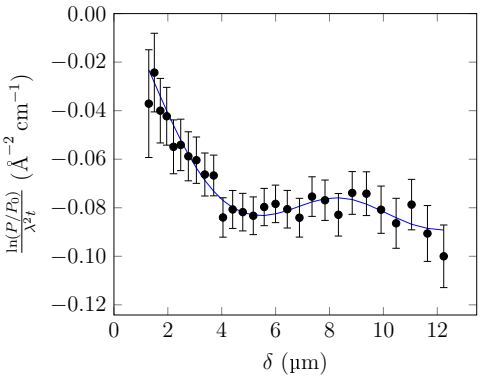

(a) Fitted SESANS signal after 1.6 hours. Scale $= 1-\phi = 0.78$, $R = 4.04\,\mu\text{m}$.

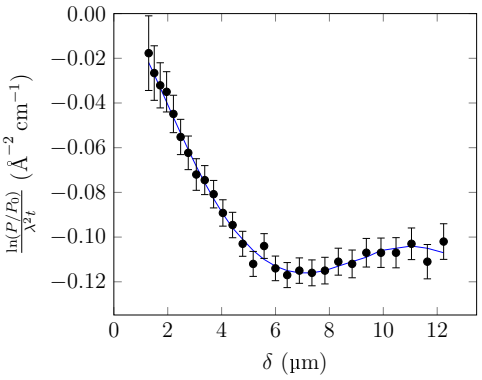

(b) Fitted SESANS signal after 5.8 hours. Scale $= 1-\phi = 0.83$, $R = 5.32\,\mu\text{m}$.

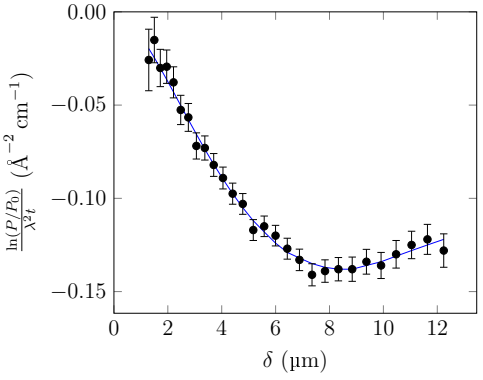

(c) Fitted SESANS signal after 10.7 hours. Scale $= 1-\phi = 0.78$, $R = 6.49\,\mu\text{m}$.

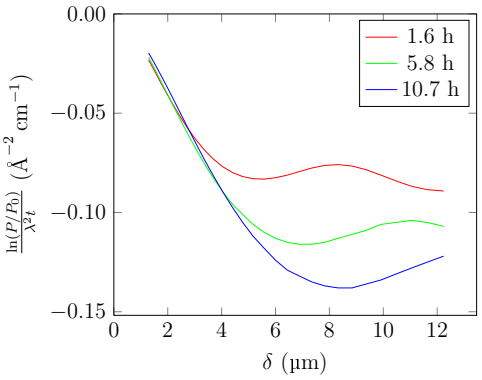

(d) The fitted lines of the three time points for comparison.

Figure 4.8: Fitted SESANS signals for sample 1 at (a) 1.6, (b) 5.8 and (c) 10.7 hours after preparation, with (d) the three fits plotted on the same figure. The data was fitted with a polydisperse sphere model and a hard-sphere structure factor. At later times, the saturation point is at higher δ and at lower polarisation. Note that, since $\phi \approx 0.5$, the scale factor ideally should equal 0.5.

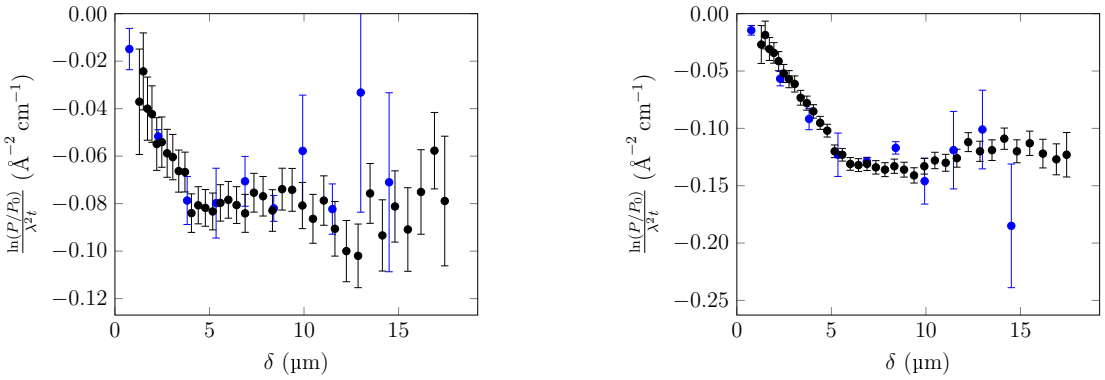

Figure 4.9: Comparison between data obtained on Larmor (black) and the Delft SESANS instrument (blue). The Delft data was rescaled to account for the difference in scattering contrast between the samples. The measurements broadly agree, but the statistical information of the data obtained at ISIS is higher than in Delft. In Delft, measurements at fewer spin-echo lengths were possible due to the shorter wavelength used and the fact that it is a monochromatic rather than a time-of-flight instrument.

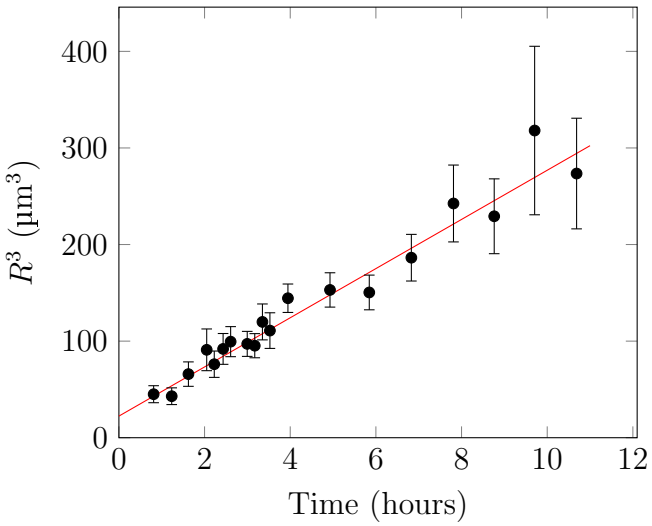

Figure 4.10: Sample 1. The cube of the mean droplet radius obtained from fitting a concentrated polydisperse sphere model is plotted against time. The ripening rate of the droplets is 25.45 µm^3 h^{-1} ($\pm$2.05, $\chi^2 = 0.50$).

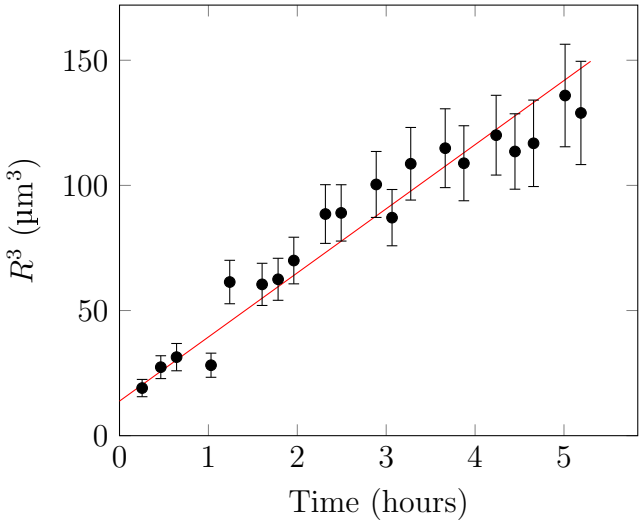

Figure 4.11: Sample 3. The cube of the mean droplet radius obtained from fitting a concentrated polydisperse sphere model is plotted against time. The ripening rate of the droplets is 25.62 µm^3 h^{-1} ($\pm$1.47, $\chi^2 = 1.01$).

seen in figures 4.12a and 4.12b, it varies between 0.65 and 0.85 for sample 1 and 0.75 and 1 for sample 3.

The width of the distribution can be expressed as the standard deviation, as given by the square root of the variance calculated from equation (3.22). For sample 1 (figure 4.13a), it is difficult to observe a trend, but sample 3 (figure 4.13b) clearly shows an increase in the standard deviation of the size distribution. The size distribution at three time points is plotted in figure 4.14. A slight broadening can be seen, but the distribution stays quite narrow.

The same analysis was done on the data measured in Delft and plotted in figure 4.15. Due to the smaller number of spin-echo length points in each measurement, the information on the polydispersity is very poor, as can be seen in figure 4.15c. The information on the time evolution of $\bar{R}^3$ is better, with a measured ripening rate of 14.1 µm^3 h^{-1}. This is considerably lower than the value obtained from the measurements done on Larmor. Multiple differences of the experimental conditions could have caused this, such as a different temperature, a different speed of the sample rotator or the different shape of the cuvette.

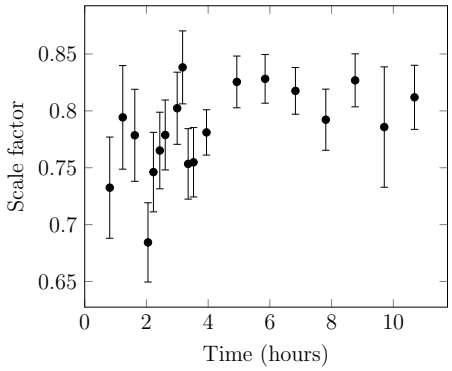

(a) Sample 1. The scale factor does not show a clear trend.

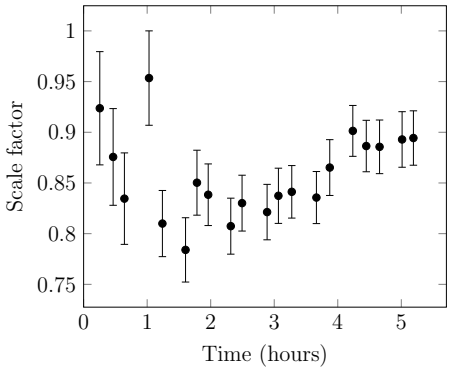

(b) Sample 3. The scale factor does not show a clear trend.

Figure 4.12: The scale factor obtained by fitting a concentrated polydisperse sphere model tot the SESANS data. If the concentration, scattering length density contrast, volume fraction, particle form factor and structure factor are all correct, this should be constant and equal to $1 - \phi = 0.5$.

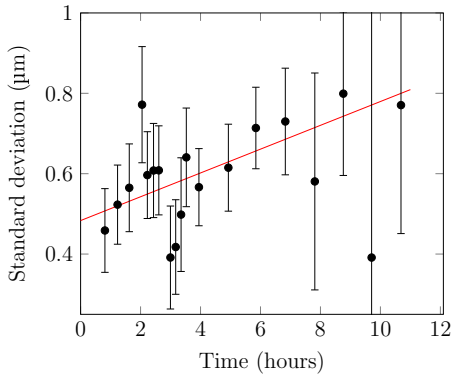

(a) Sample 1. The trend is not very clear. A line was fitted with slope $0.030\,\mu\mathrm{m\,h^{-1}}$ (± 0.015, $\chi^2 = 0.52$).

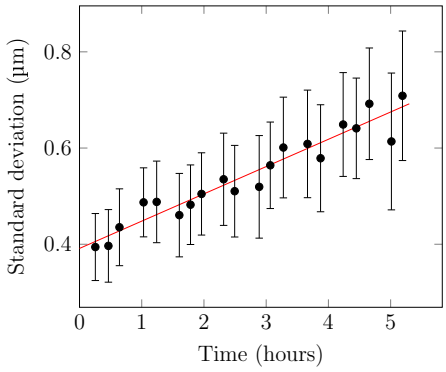

(b) Sample 3. A clear linear upward trend with a slope $0.057\,\mu\mathrm{m\,h^{-1}}$ (± 0.014, $\chi^2 = 0.07$).

Figure 4.13: The standard deviation of the particle size distribution obtained by fitting a concentrated polydisperse sphere model tot the SESANS data. During Ostwald ripening, this standard deviation increases with time.

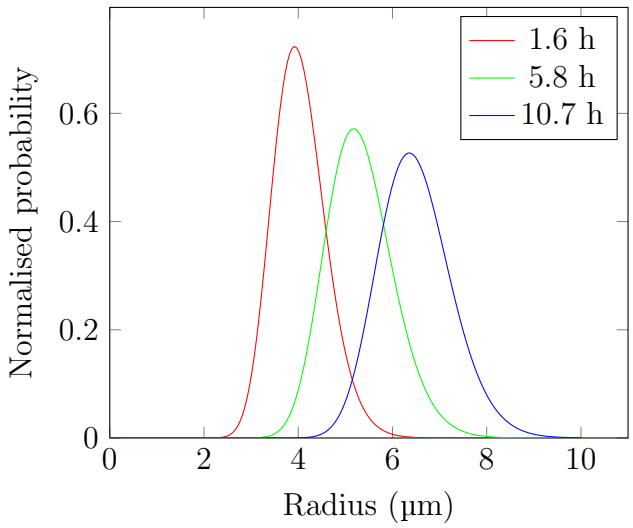

Figure 4.14: The radius distributions obtained from the fitting the data in figure 4.8. The data is fitted using a polydisperse sphere model where the radius is distributed according to the log-normal distributions shown.

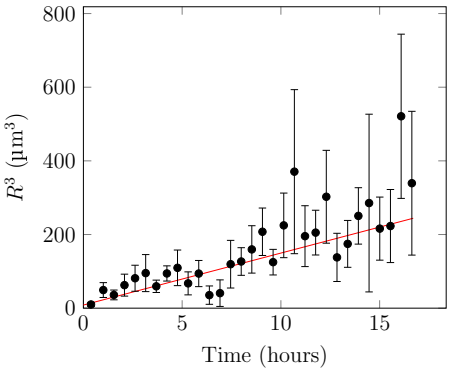

(a) Radius cubed

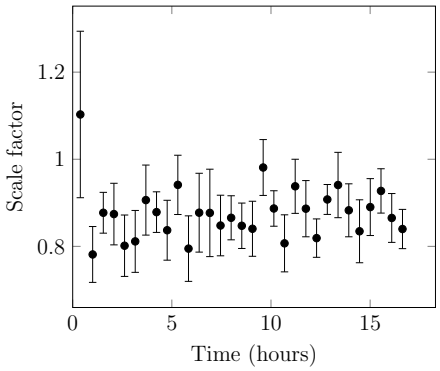

(b) Scale factor

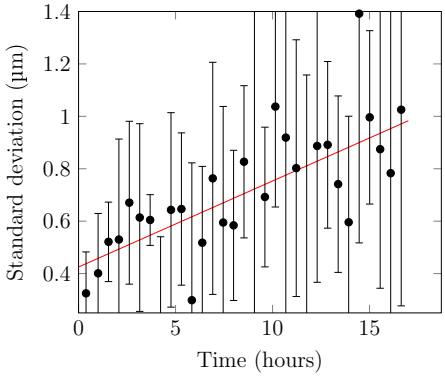

(c) Standard deviation

Figure 4.15: The time evolution of (a) the mean radius cubed ($\bar{R}^3$), (b) scale factor and (c) standard deviation as measured on the Delft SESANS instrument and fitted using a concentrated polydisperse sphere model. The radius cubed increases with 14.1 µm^3 h^{-1} ($\pm$1.44, $\chi^2 = 0.85$). Due to the small number of spin-echo length points in the measurements, the data on the standard deviation of the size distribution is extremely poor. It can be fitted with a line with a slope of 0.034 µm h^{-1} ($\pm$0.012, $\chi^2 = 0.19$).

Chapter 5

Conclusion

The presented results from the SESANS measurements show that the mean droplet size of decane-in-DMSO emulsions grows with a linear relation between $\bar{R}^3$ and time. The width of the size distribution increases slightly, but the emulsions stay relatively monodisperse. It is difficult to exactly determine the dominant process in this coarsening. Flocculation, Ostwald ripening and coalescence with particle collisions as the rate-limiting step all result in a linear increase of $\bar{R}^3$ with time. In Imhof and Pine's [15] study into the stability of this and other non-aqueous emulsions, they found a significant increase in the stability when a small amount of silicone oil was added to the decane. This effectively stops Ostwald ripening, but does not influence the other processes. It is therefore reasonable to assume that Ostwald ripening is the main driver of droplet growth. In surfactant-free conditions, equation (2.8) can be used to calculate the ripening rate of a decane-in-DMSO emulsion. Substituting the relevant values, a rate of $1.73\,\mu m^3\,h^{-1}$ is obtained. However, Koroleva and Yurtov [10] remark in their review that, in most publications, the Ostwald ripening rates are considerably higher when the surfactant concentration is greater than the critical micelle concentration. The SESANS measurements confirm this.

Ostwald ripening is usually associated with a much larger increase in the width of the size distribution than observed using SESANS. One effect could be the presence of a large number of swollen micelles, as evidenced by the SANS measurement. Smaller droplets might be unstable enough to shrink quickly or fall apart into swollen micelles. However, the SANS data does not show an increase in the number of micelles. The distribution obtained mathematically from the Lifshitz-Slyozov-Wagner theory describing Ostwald ripening (equation (2.9)) does have a constant (relative) width, more in line with what is measured. This theoretical distribution is still broader than the distributions fitted. Fitting the data using this distribution rather than a

log-normal one does not yield good results.

Another effect that should be considered is the dependency of the scattering on the particle volume. If the distribution is not monomodal, the scattering is dominated by the larger particles and any smaller populations may be missed. In the microscopy image of a 20 hour old emulsion (figure 4.2b) a population of smaller droplets is visible in addition to the larger ones. This may indicate a bimodal distribution of droplet sizes. However, it is important to note that the procedure of preparing the emulsion for microscopic imaging involves a high degree of dilution, in addition to being pipetted twice. This could have an effect on the emulsion and hence on how representative the microscopy pictures are for the emulsion in its 'natural' state.

From the measurements presented in this thesis, it is difficult to determine what influence the swollen surfactant micelles, measured by SANS, have on the ripening process. It is also not possible to distinguish Ostwald ripening from other processes which may be taking place at the same time, if those processes result in the same growth behaviour. SESANS measurements on emulsions with a small amount of silicone oil added could give insight in the role of flocculation and coalescence in the ripening process. A series of measurements with different surfactant concentrations and decane volume fractions could give insight into how these quantities affect the ripening rate and therefore the relative importance of different growth mechanisms.

Appendix A

Appendix

A.1 Pluronic P-68

Originally, emulsions stabilised by another Pluronic surfactant, P-68 (also known as Poloxamer 188), were also planned to be investigated. This surfactant is similar to P-123, but with longer solvophilic blocks (PEGLPPG:PEG = 76:29:76). Decane-in-DMSO emulsions made with this surfactant have a shorter time-until-breaking and hence it was expected that the kinetics would be on a shorter time scale than the P-123 emulsions.

The same approach as for P-123 was used to perform the SESANS measurements: the scattering length density of the DMSO was chosen close to that of P-68 ($0.580 \times 10^{-6}\,\text{Å}^{-2}$). Three different samples were made with different scattering contrasts of the decane with the DMSO. The results are summarised in figure A.2. If the contrast is too high (sample 1), the neutron beam completely depolarises at even moderate spin-echo lengths. If the contrast is decreased, depolarisation becomes less of an issue, but still no plateau region is reached within the measurable range of the instrument. Because of this, it was not possible to determine the size of the droplets in these emulsions. From the microscopy image in figure A.1 it can be seen that they are too large for SESANS to measure.

A.2 Monodisperse sphere fits

The model described in section 3.5.1 to fit the SESANS data is rather complex, since it involves a size distribution and a structure factor. This necessitates approximations such as the decoupling approximation and Percus-Yevick closure described. It is therefore tempting to simplify even further: assume the data can be fitted with a simple monodisperse sphere with a structure factor

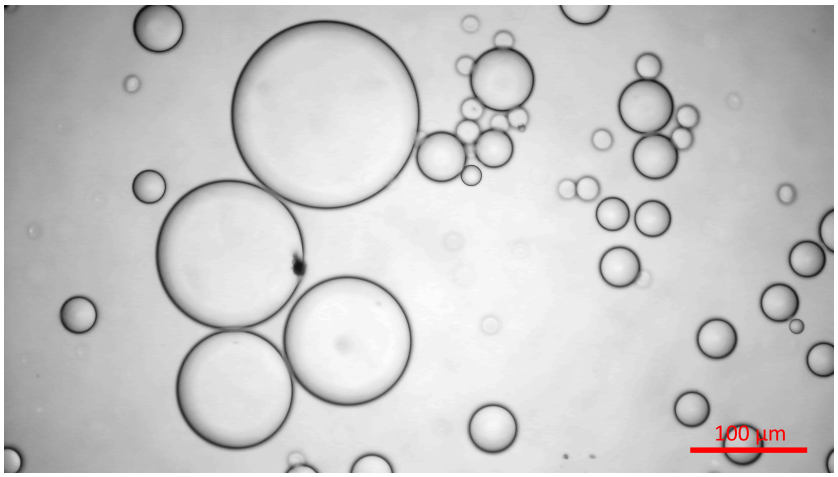

Figure A.1: Microscopy image of a decane-in-DMSO emulsion stabilised by Pluronic P-68. Very large droplets are visible, much larger than the range measurable by SESANS.

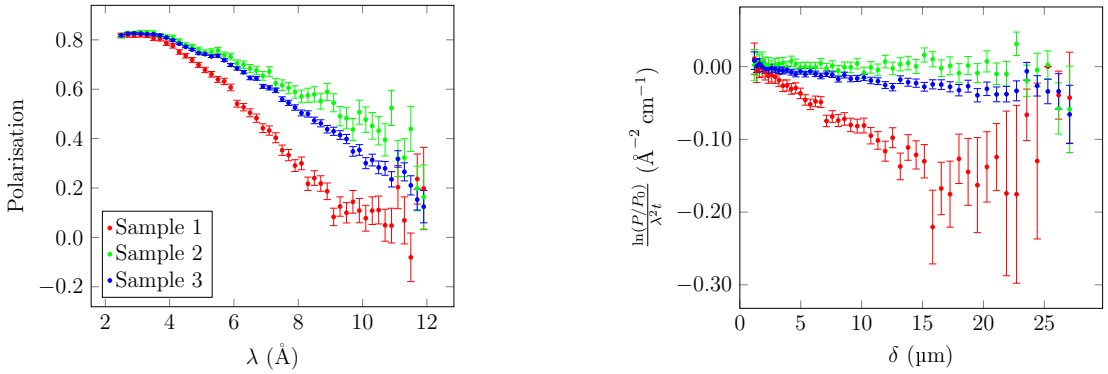

Figure A.2: The results from Larmor SESANS measurements on decane-in-DMSO emulsions stabilised by Pluronic P-68. Three different contrasts were measured.

that is constant over the entire range of spin-echo lengths. In figure A.3, three SESANS signals at three different time points are fitted in this way. While the quality of the fits is decent, at the two later times there is a clear dip in the signal (due to the structure factor) that this model does not account for. Since this feature is consistently present in the measured data, it was decided that the more complicated polydisperse model should be used.

The dilute monodisperse model always gives smaller values of the radius then the polydisperse model. This is an effect of the structure factor and another reason this factor should explicitly be taken into account when fitting the data. The growth of the radius cubed in time does give a linear relation, but with a slower ripening rate (figure A.4). It is unclear how this radius relates to the size distributions obtained from fitting the polydisperse model.

A.3 Dynamic Light Scattering

The emulsion was diluted and measured using a Malvern Zetasizer Nano S. Access to this DLS instrument was provided by the biological support laboratory at ISIS. The results of one such measurement, on an emulsion measured 50 minutes after preparation, is given in figure A.5. The resulting size distribution has a number of peaks between 100 and 10 000 nm. It is therefore likely that particles in a broad size range are present in the emulsion. However, neither the position of these peaks nor the existence of multiple peaks was reproducible. The emulsions are too polydisperse to measure accurately. Additionally, the diluted emulsion creams quickly and therefore the droplet sizes in the measured volume (about halfway in the cuvette) change quickly.

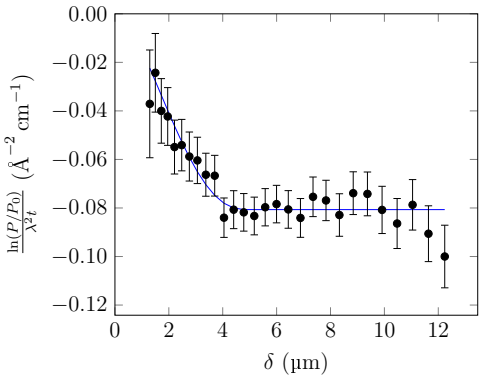

(a) Fitted SESANS signal after 1.6 hours. $R = 2.4\,\mu m$.

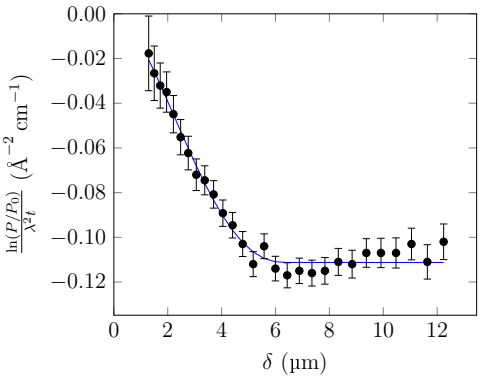

(b) Fitted SESANS signal after 5.8 hours. $R = 3.2\,\mu m$.

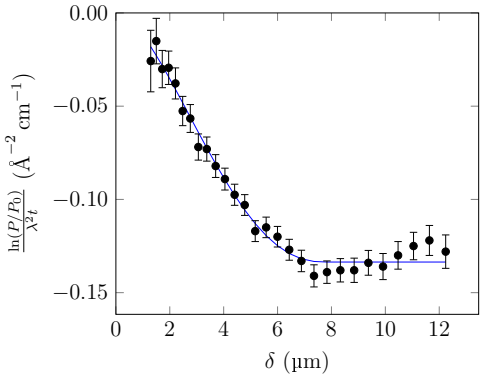

(c) Fitted SESANS signal after 10.7 hours. $R = 3.9\,\mu m$.

Figure A.3: SESANS measurements at three different time points, fitted with a dilute monodisperse sphere model.

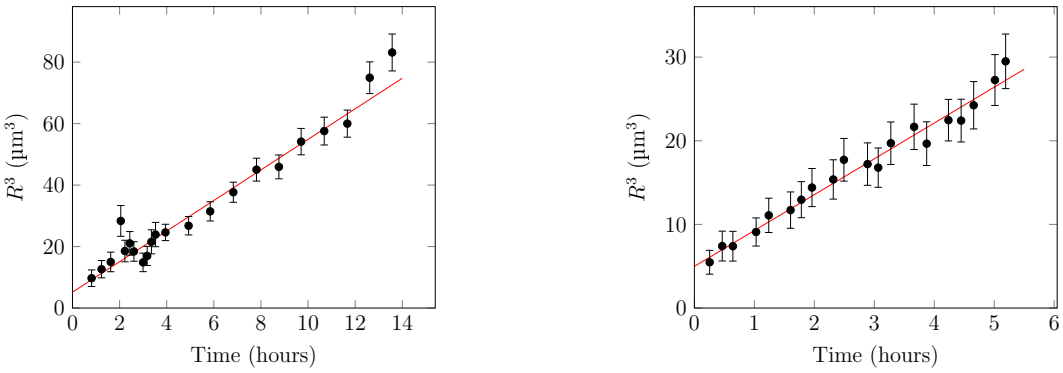

(a) Sample 1 (b) Sample 3

Figure A.4: The cube of the radius obtained from the monodisperse sphere fits plotted against time. The ripening rates are 5.0 µm^3 h^{-1} (±0.2) for sample 1 and 4.3 µm^3 h^{-1} (±0.3) for sample 3.

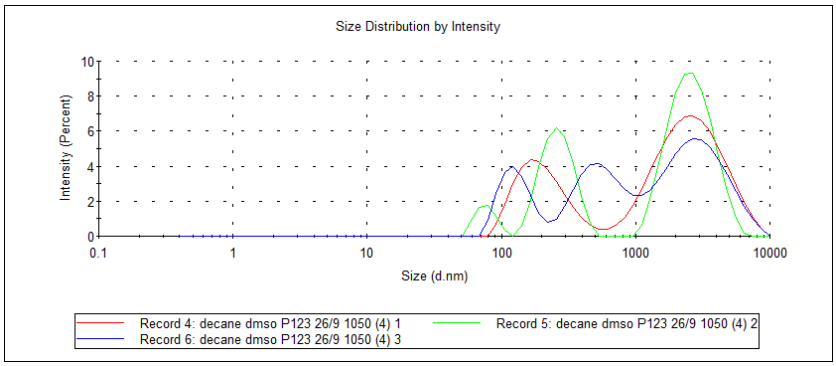

Figure A.5: Intensity-weighted size distribution obtained by DLS from an emulsion 50 minutes after preparation. The three curves represent three separate measurements taken within 5 minutes on the same sample. Due to the high polydispersity and creaming of the sample, the size distribution obtained is highly unreliable.

Bibliography

[1]D. J. McClements, *Food emulsions, Principles, practices, and techniques*, 2nd edition (CRC Press, Boca Raton, 2004).

[2]A. Imhof and D. J. Pine, "Ordered macroporous materials by emulsion templating", Nature, 948 –951 (1989).

[3]A. Zia, E. Pentzer, S. Thickett, and K. Kempe, "Advances and opportunities of oil-in-oil emulsions", ACS applied materials & interfaces **12**, 38845–38861 (2020).

[4]C. Rehm, J. Barker, W. G. Bouwman, and R. Pynn, "DCD USANS and SESANS: a comparison of two neutron scattering techniques applicable for the study of large-scale structures", Journal of Applied Crystallography **46**, 354–364 (2013).

[5]B. Vincent, "Emulsions", in *Colloid science: principles, methods and applications*, edited by T. Cosgrove, 2nd edition (John Wiley, Chichester, 2010) Chap. 6, pp. 117 –133.

[6]J. Eastoe, "Micromulsions", in *Colloid science: principles, methods and applications*, edited by T. Cosgrove, 2nd edition (John Wiley, Chichester, 2010) Chap. 5, pp. 91 –115.

[7]D. F. Evans and H. Wennerstrom, *The colloidal domain, Where physics, chemistry, biology and technology meet* (VHC Publishers, New York, 1996).

[8]C. Wagner, "Theorie der Alterung von Niederschlägen durch Umlösen (Ostwaldreifung)", Zeitschrift für Elektrochemie **65**, 581–591 (1961).

[9]T. Sakai, K. Kamogawa, K. Nishiyama, H. Sakai, and M. Abe, "Molecular diffusion of oil/water emulsions in surfactant-free conditions", Langmuir **18**, 1985–1990 (2002).

[10]M. Y. Koroleva and E. V. Yurtov, "Ostwald ripening in macro-and nanoemulsions", Russian Chemical Reviews **90**, 293–323 (2021).

[11]S. Maaref and S. Ayatollahi, "The effect of brine salinity on water-in-oil emulsion stability through droplet size distribution analysis: a case study", Journal of Dispersion Science and Technology **39**, 721–733 (2018).

[12]A. M. Djerdjev and J. K. Beattie, "Enhancement of ostwald ripening by depletion flocculation", Langmuir **24**, 7711–7717 (2008).

[13]"The formation and ageing rates of oil-in-water miniemulsions", Colloids and Surfaces A **88**, 303–316 (1994).

[14]A. S. Kabalnov, "Can micelles mediate a mass transfer between oil droplets?", Langmuir **10**, 680–684 (1994).

[15]A. Imhof and D. J. Pine, "Stability of nonaqueous emulsions", Journal of Colloid and Interface Science **192**, 368 –374 (1997).

[16]J. Schindelin, I. Arganda-Carreras, E. Frise, V. Kaynig, T. Pietzsch, S. Preibisch, C. Rueden, S. Saalfeld, B. Schmid, J.-Y. Tinevez, D. J. White, V. Hartenstein, K. Eliceiri, P. Tomancak, and A. Cardona, "Fiji: an open-source platform for biological-image analysis", Nature Methods **9**, 676 –682 (2012).

[17]P. Debye, "Molecular-weight determination by light scattering.", The Journal of Physical and Colloid Chemistry **51**, 18–32 (1947).

[18]J. Kohlbrecher and I. Breßler, "Updates in *SASfit* for fitting analytical expressions and numerical models to small-angle scattering patterns", Journal of Applied Crystallography **55**, 1677–1688 (2022).

[19]M. T. Rekveldt, J. Plomp, W. G. Bouwman, W. H. Kraan, S. Grigoriev, and M. Blaauw, "Spin-echo small angle neutron scattering in Delft", Review of Scientific Instruments **76**, 033901 (2005).

[20]W. G. Bouwman, "Spin-echo small-angle neutron scattering for multiscale structure analysis of food materials", Food Structure **30**, 100235 (2021).

[21]R. Anderson, L. F. van Heijkamp, I. M. de Schepper, and W. Bouwman, "Analysis of spin-echo small-angle neutron scattering", Journal of Applied Crystallography **41**, 868–885 (2008).

[22]T. Kruglov, "Spin-echo small-angle neutron scattering for dense systems of spheres", Journal of Applied Crystallography **38**, 721–726 (2005).

[23]J. H. Bakker, A. L. Washington, S. R. Parnell, A. A. van Well, C. Pappas, and W. G. Bouwman, "Analysis of SESANS data by numerical Hankel transform implementation in SasView", Journal of Neutron Research **22**, 57–70 (2020).

[24]A. Guinier and G. Fournet, *Small-angle scattering of x-rays*, trans. by C. B. Walker (John Wiley, New York, 1955).

[25]S. King and P. Kienzle, *Polydispersity and orientational distributions*, version 3 November 2021, SasView, (2015) `https://www.sasview.org/docs/user/qtgui/Perspectives/Fitting/pd/polydispersity.html`.

[26]J. A. Boxall, C. A. Koh, E. D. Sloan, A. K. Sum, and D. T. Wu, "Measurement and calibration of droplet size distributions in water-in-oil emulsions by particle video microscope and a focused beam reflectance method", Industrial and Engineering Chemistry Research **49**, 1412—1418 (2010).

[27]J.-P. Hansen and I. R. McDonald, *Theory of simple liquids* (Elsevier, Amsterdam, 2006).

[28]J. K. Percus and G. J. Yevick, "Analysis of classical statistical mechanics by means of collective coordinates", The Physical Review **110**, 1–13 (1958).

[29]N. W. Ashcroft and J Lekner, "Structure and resistivity of liquid metals", Physical Review **145**, 83–90 (1966).

[30]M. Kotlarchyk and S. Chen, "Analysis of small angle neutron scattering spectra from polydisperse interacting colloids", The Journal of Chemical Physics **79**, 2461–2469 (1983).

[31]J. Plomp, V. de Haan, R. Dalgliesh, S. Langridge, and A. van Well, "Neutron spin-echo labelling at offspec, an isis second target station project", Thin Solid Films **515**, 5732–5735 (2007).

[32]I. Grillo, "Small-angle neutron scattering and applications in soft condensed matter", in *Soft matter characterization*, edited by R. Borsali and R. Pecora (Springer, Dordrecht, 2008), pp. 723–782.

[33]K. Dehvari, K.-S. Lin, and B. Hammouda, "Small-angle neutron scattering studies of microenvironmental and structural changes of pluronic micelles upon encapsulation of paclitaxel", Journal of the Taiwan Institute of Chemical Engineers **71**, 405–413 (2017).

[34]SasView, *Sasview for small angle scattering analysis*, (2023) `https://www.sasview.org`.